AGU ADVANCING EARTH AND SPACE SCIENCES

Geophysical Research Letters

RESEARCH LETTER
10.1029/2025GL118710

New Li Lidar Observations and Model Simulations: A Window to Anthropogenic Signatures

M. Gerding[1], R. Wing[1], W. Feng[2,3], J. M. C. Plane[4], and G. Baumgarten[1]

[1]Leibniz-Institute of Atmospheric Physics at University Rostock, Kühlungsborn, Germany, [2]National Centre for Atmospheric Science, University of Leeds, Leeds, UK, [3]School of Earth and Environment, University of Leeds, Leeds, UK, [4]School of Chemistry, University of Leeds, Leeds, UK

Key Points:

- Rare observations of the upper mesospheric Li layer were performed by mid-latitude lidar
- The new WACCM-Li model satisfactorily reproduces the Li seasonal variation, but some high density events in January/February 2025 remain unexplained
- Li observations have a great potential for studying ablation of re-entering space debris and its impact on atmospheric composition

Supporting Information:

Supporting Information may be found in the online version of this article.

Correspondence to:

M. Gerding,
gerding@iap-kborn.de

Citation:

Gerding, M., Wing, R., Feng, W., Plane, J. M. C., & Baumgarten, G. (2025). New Li lidar observations and model simulations: A window to anthropogenic signatures. *Geophysical Research Letters*, *52*, e2025GL118710. https://doi.org/10.1029/2025GL118710

Received 5 AUG 2025
Accepted 10 OCT 2025

Abstract We present Li lidar observations in the mesopause region above Kühlungsborn, Germany (54°N, 12°E). The lithium layer is mainly formed by meteoric ablation. But lithium has a much higher relative abundance in space debris compared with meteoroids, making it a good indicator of anthropogenic influence in the upper mesosphere. Our measurements reveal a strong seasonal increase in Li abundance between August and December 2024, growing from $\sim 1.6 \times 10^6$ to 4.7×10^6 cm^{-2}. These values are in reasonable agreement with the first simulations based on the Whole Atmosphere Community Climate Model (WACCM6) with a newly developed Li chemistry network; however, WACCM-Li does not explain high Li abundances of up to 10.7×10^6 cm^{-2} observed in January/February 2025. This may be due to anthropogenic effects or an unidentified natural mechanism. This study highlights the potential of lithium observations for monitoring the consequences of re-entering space debris on the composition of the atmosphere.

Plain Language Summary We have studied the amount of lithium in the upper atmosphere above Germany using a special laser system. Lithium is a key component of space debris, which is made up of old satellites and rocket parts. Because of this, lithium is a good indicator of whether human activities are affecting the upper atmosphere. Our measurements show that the amount of lithium in the upper atmosphere increases significantly during the autumn and early winter months. These results are in line with computer simulations that predict how much lithium should be in the upper atmosphere from natural sources. However, the simulations cannot explain why we saw such high levels of lithium in early 2025. This could be due to the breakdown of space debris in the atmosphere, or it could be a natural phenomenon that we have not yet accounted for. Our study shows that measuring lithium in the upper atmosphere can help us understand the impact of space debris on the environment.

1. Introduction

Metallic species, including atoms, molecules, ions, and clusters/aerosols, are ubiquitous in the Earth's atmosphere, resulting from the ablation of meteoroids in the mesosphere and lower thermosphere (Plane et al., 2015). However, Murphy et al. (2023) recently observed the contamination of sulfuric acid droplets in the lower stratospheric Junge layer by metals that are not abundant in cosmic dust. Those authors concluded that these metals originate from the ablation of anthropogenic space debris. The mass-flux of re-entering satellites and space debris is continuously increasing, and its impact on the composition of the atmosphere is gaining increasing attention (Barker et al., 2024; Boley & Byers, 2021; Ferreira et al., 2024; Schulz & Glassmeier, 2021). Many studies are based on theoretical expectations and model simulations, while direct observations of the ablation of space debris are sparse and limited to a few dedicated experiments (see, e.g., review by Zander and Löhle (2025)). Therefore, there remains a large uncertainty concerning the possible effects of re-entering satellites and rocket stages on the atmosphere.

Li is one of the species detected in the stratosphere attributed to anthropogenic injections, and most likely comes from the Li-Al alloys used in satellite and rocket bodies and the Li batteries of re-entering objects. On the other hand, however, Li is also an naturally-occurring element in the upper mesospheric atomic metal layers, that are generated by meteoric ablation between about 80 and 110 km altitude. The various metal layers have been studied for decades to understand their chemistry and as tracers of the dynamics of this important region at the edge of space. The first Li observations were performed by spectroscopic measurements during twilight (e.g., Gadsden & Salmon, 1958; Sullivan & Hunten, 1962). Later, active experiments by lidar provided a significantly improved altitude resolution as well as temporal resolution, with soundings not being limited to twilight conditions. The only Li observations by lidar so far have been published by Jegou et al. (1980, 1985), covering data from Observatoire de Haute-Provence (OHP, 44°N, 6°E) in the years 1977–1982. Subsequent lidar observations of mesospheric metals focused on sodium, potassium, iron, calcium, and recently also nickel (e.g., Chu et al., 2011; Gerding et al., 2019; Guo et al., 2017; Höffner & Lautenbach, 2009; Huang et al., 2015; Lautenbach et al., 2017; Wu et al., 2021), mainly to understand the seasonal variation and chemical variability, magnitude of the cosmic dust input and small-scale dynamics by targeting Doppler temperature and wind measurements. Increasing signal-to-noise ratios have allowed observations to be extended into the thermosphere (e.g., Chen & Chu, 2023; Chu et al., 2011). An overview of the observed mesospheric metals and their particular chemical reaction schemes can be found in the review by Plane et al. (2015).

Compared to other metals, Li is potentially the best indicator for the additional anthropogenic input in the mesopause region. The mass fraction of Li in typical satellites and rocket bodies is much higher than the natural abundance in meteoroids. In this paper we will describe the first Li measurements in the mesopause region since 1982. We will compare the observed abundance of Li with the predicted abundance from natural sources as simulated by the first global model of meteoric lithium (WACCM-Li). This will set a baseline for future regular Li soundings to monitor the influence of increasing amounts of space debris on the middle atmosphere. In Section 2, we describe our lidar instrument and the Li observations, and in Section 3 the Li model with a detailed chemistry network. In Section 4, we compare model results and observations, followed by the Discussion and Conclusions in Section 5.

2. Description of the Lidar and the Li Observations

2.1. Description of the Li Lidar and Data Processing

Part of the lidar system used for the Li soundings has already been described by Gerding et al. (2019) for nickel detections. We repeat the main properties of the system and describe the difference from the earlier lidar. The system is located at Kühlungsborn, Germany (54°N, 12°E). The transmitter consists of an XeCl-excimer laser running now at a 50 pps repetition rate, pumping a dye laser. The laser is triggered with a fixed offset relative to the lasers of our Rayleigh-Mie-Raman (RMR) lidars (Gerding et al., 2016, 2024) to avoid any potential influence from the strong tropospheric backscatter of the RMR lidars on the weak signal of the Li lidar. The dye laser operates on DCM dye (4-(Dicyanomethylene)-2-methyl-6-(4-dimethylaminostyryl)-4H-pyran) dissolved in propylene carbonate, emitting light at a wavelength of $\lambda_{air} = 670.7926$ nm. The average pulse energy is ~5 mJ. The bandwidth of the dye laser at this wavelength is ~1.5 p.m., limited by an intra-cavity etalon. The resonator of the laser is temperature-stabilized to achieve a constant wavelength, and the wavelength is regularly checked with a wavemeter (Bristol Instruments 371A). A beam expansion telescope limits the divergence of the beam to 0.5 mrad. The backscattered light is collected by a 78 cm telescope mirror and finally detected by an Avalanche Photo Diode (Excelitas SPCM-AQRH 16). Background light from the sky (moon, etc.) is suppressed by an interference filter with a bandwidth of 2.7 nm and a transmission at maximum of 85%. Backscattered photons are integrated over 4,000 pulses (i.e., 80 s) with an altitude resolution of 200 m. Typically, further integration over, for example, 1 hr was needed to achieve a sufficient signal-to-noise ratio.

We probed the Li resonance transition $1s^22s$-$1s^22p$. Spectroscopic data for this transition are taken from Wiese and Fuhr (2009) and the NIST tabulated data (NIST, 2025). From these data we calculated an effective resonance and Rayleigh backscatter cross section of $\sigma_{res} = 2.047 \times 10^{-17}$ m^2sr^{-1} and $\sigma_{Ray} = 2.384 \times 10^{-32}$ m^2sr^{-1}, respectively, for our laser (Fricke & von Zahn, 1985; Chu & Papen, 2005). The first night of Li soundings was used to verify the spectroscopic data and the accuracy of the wavelength measurement. For this we tuned the laser by about ±1 p.m. around the expected wavelength and integrated the signal over about 1 hr at each wavelength. The largest signal was acquired at $\lambda_{air} = 670.7926$ nm, which equals the wavelength of the upper line of the doublet $1s^22s$-$1s^22p$ as given by NIST (2025). The wavelength is slightly different from the reference published by Wiese and Fuhr (2009) ($\lambda_{air} = 670.791$ nm) and recent spectroscopic measurements by Phillips et al. (2025) ($\lambda_{air} = 670.7917$ nm). Given the large statistical uncertainty of the lidar soundings, we cannot finally confirm from our data which wavelength is correct. The figures in this paper therefore include a potential underestimate of the density by up to 20%. For simplicity, the numbers given in the following text describe only the statistical uncertainty from photon counting, assuming Poisson statistics, which adds to this systematic uncertainty. We are

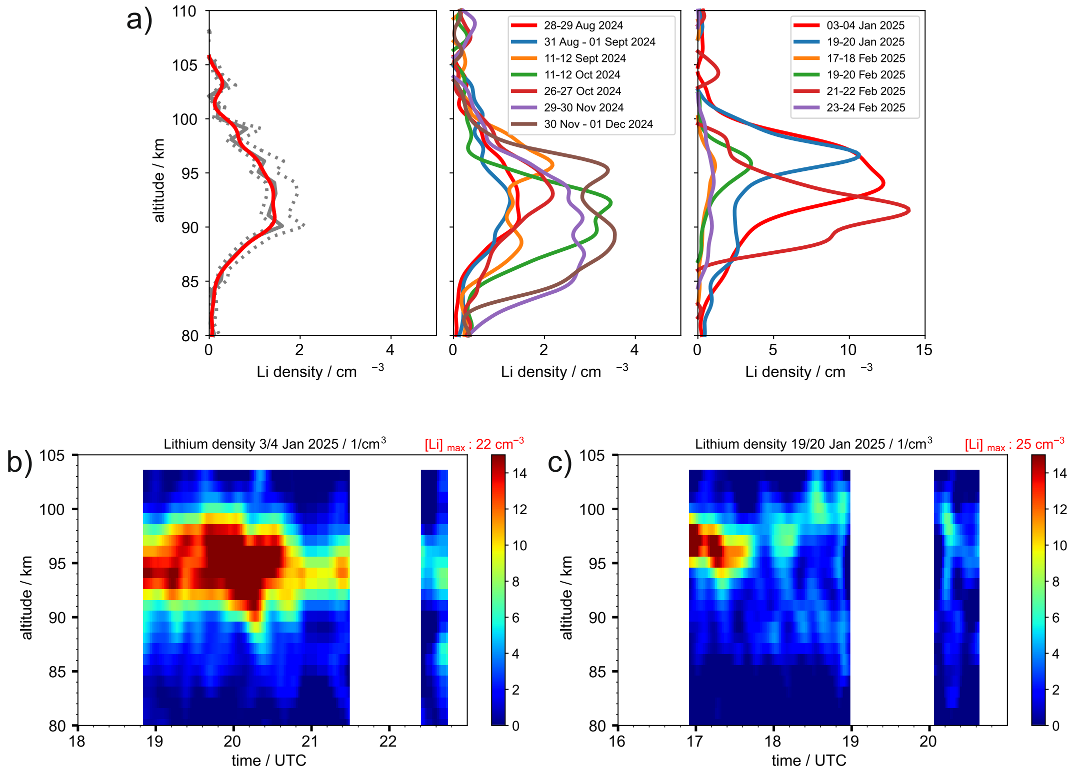

Figure 1. (a) Nightly mean observed Li density profiles. Left: 28/29 August 2024, profiles with 1 km binning (gray solid) and uncertainties (gray dotted) and smoothed profile (red). Centered: All profiles August–December 2024, smoothed. Right: All profiles January–February 2025, smoothed. Smoothed profiles are calculated with 200 m binning and smoothed by 21-bin Hann window. (b and c) Temporally resolved Li soundings on 3 January 2025 (b) and 19 January 2025 (c). The resolution is 80 s by 1 km vertical. A 2d Hann window (7 bins, 15 profiles) is applied for smoothing.

currently installing a new laser system to continue the Li observations with a much improved signal-to-noise ratio, which will allow us also studies of the Li resonance wavelengths.

The Li number density is calculated from the backscatter profile by

$$\rho_{Li}(z) = \rho_{air}(z_R) \cdot \sigma_{Ray}/\sigma_{res} \cdot N_{res}^{corr}(z)/N_{Ray}^{corr}(z_R)$$

with the range-corrected resonance count rate N_{res}^{corr}, the range-corrected Rayleigh count rate $N_{Ray}^{corr}(z_R)$ at the reference altitude z_R (here: 50 km), and the air density $\rho_{air}(z_R)$ at the reference altitude as given by an empirical global reference model NRLMSISE-00 for Earth's atmosphere (Picone et al., 2002).

2.2. Nightly Mean Profiles and Examples of Time-Resolved Observations

The first measurement of mesospheric Li at our site was performed on the night of 28/29 August 2024. Figure 1a shows left the Li density profile after integration over ~430,000 laser pulses, that is, about 2:45 hr. The gray profile shows the unsmoothed data in 1 km bins with its statistical uncertainty. The red profile is based on the original resolution of 200 m, but smoothed by a 21-bin Hann window (full width at half maximum is 2.1 km). The Li layer starts at about 85 km altitude and exhibits a broad maximum between 90 and 94 km altitude with a peak density of 1.4 ± 0.2 atoms cm^{-3}. The Li density goes to zero at ~105 km altitude.

Overall, seven soundings were performed between August and December 2024. The smoothed mean profiles are summarized in Figure 1a (center panel). The second sounding during the evening of 31 August 2025 showed a similar layer shape and a similar peak density of ~1.3 cm^{-3}. In mid-September the Li abundance started to increase. The layer shapes during autumn were highly variable, particularly below 90 km where the Li concentration changed dramatically between observations (e.g., in October). On the night 30 November/1 December

2024, a maximum of 3.6 cm^{-3} at 89 km and a secondary maximum of 3.4 cm^{-3} at 95 km altitude were observed. Observations in 2025 started with the largest Li density detected so far (Figure 1a, right-hand panel): On the night of 3/4 Jan 2025, we found a peak density of 12.2 cm^{-3} at 94 km. As in the soundings in 2024, the Li layer shape remained highly variable during January/February 2025. The largest concentration was observed on the night of 21/22 February 2025 (13.9 cm^{-3} at ∼92 km), directly followed by the lowest peak density (1.1 cm^{-3} at ∼94 km) two nights later on 23/24 February 2024.

About 1 hr of measurements is needed to resolve layers with peak densities around 1 cm^{-3}. The high density in the two soundings in January 2025 enables a time-resolved study of the Li layer. Figures 1b and 1c shows the time-resolved Li density for the evenings of 3 and 19 January 2025, respectively. Both data sets suffer from some cloud coverage that interrupted and finally terminated the lidar soundings. At the beginning of the sounding on 3 January 2025, the Li density had already reached more than 12 cm^{-3} around 95 km altitude. Over the next hour, the density increased further up to ∼22 cm^{-3}. After ∼20:30 UTC the density quickly decreased again and remained at 6–10 cm^{-3} until the end of the sounding. The last profiles of that night show indications of a double layer with an additional lower maximum at ∼86 km altitude. The next sounding was performed about two weeks later on 19 January 2025. Here the first profiles also already showed a high Li density of 20–25 cm^{-3} at 95–97 km altitude. On this evening, the Li density quickly dropped to ∼5 cm^{-3} at 17:50 UTC, about 1 hr after the start of the sounding. In the remaining time of the sounding, a thin layer of enhanced Li concentration was observed with a center altitude of up to 100 km. In both soundings only the part of the Li layer above 90 km was enhanced, but not the layer as a whole. The peak density decreased rapidly by a factor of 4–5 within about 1 hr.

3. Description of the Lithium Chemistry Model

We have developed the first global meteoric Lithium model (WACCM-Li) by incorporating a Li meteoric ablation input function and its chemistry network (see below) in the Whole Atmosphere Community Climate Model (WACCM6) (Gettelman et al., 2019) within the CESM2 framework (Danabasoglu et al., 2020). The simulation uses specified dynamics (SD), where the model is nudged below 50–60 km with meteorological fields (temperature and winds) from Modern-Era Retrospective analysis for Research and Applications (MERRA2, Molod et al. (2015)). The horizontal resolution is 1.9° latitude by 2.5° longitude, with 88 vertical levels (Feng et al., 2013). After a five-year spin-up, the model was run for the years 2015–2019 (the latest year for which solar/geomagnetic forcing is available based on CMIP6 (Matthes et al., 2017). The model output for the location of Kühlungsborn was stored every 30 min.

The Li chemistry network used in WACCM-Li is illustrated in Figure 2. The reactions and rate coefficients used in the network are listed in Table A1 in the Appendix. Several of these rate coefficients have been measured over the temperature and pressure ranges needed to extrapolate with reasonable confidence to the conditions of the MLT (see the footnotes to Table A1). The reaction enthalpies and photodissociation thresholds were calculated using the compound G4 quantum chemistry method (Curtiss et al., 2007) within the Gaussian 16 suite of programs (Frisch et al., 2016). Details of the calculations are provided in Supporting Information S1. Table S1 in Supporting Information S1 contains the molecular parameters (geometry co-ordinates, rotational constants and vibrational frequencies) of stationary points of each reaction potential energy surfaces (PES) required to estimate its reaction rate coefficient using the Master Equation Solver for Multi-Energy well Reactions (MESMER) program (Glowacki et al., 2012), with capture rates estimated using long-range transition state theory (Georgievskii & Klippenstein, 2005). The PESs for the reactions R6 and R8 are shown in Figures S2 and S3 in Supporting Information S1, respectively. $LiHCO_3$ (lithium bicarbonate) appears to be a stable reservoir species: the three possible reaction channels of $LiHCO_3$ with atomic H have significant barriers, and are in any case endothermic (see Figure S4 in Supporting Information S1); and possible reactions with atomic O are highly endothermic.

The optical absorption cross sections for Li molecules (Figure S5 in Supporting Information S1) were calculated using time-dependent density function theory. The atomic Li photo-ionization cross section (Verner et al., 1996) is relatively large with a threshold in the near-UV (Figure S5 in Supporting Information S1), so that photo-ionization is as important as charge transfer of Li with ambient O_2^+ and NO^+ ions in the production of Li^+ ions. The photolysis rates in Table A1 were then calculated by convolving the cross section, up to the thermodynamic threshold wavelength, with the solar actinic flux from the semi-empirical SOLAR2000 model (Tobiska et al., 2000)

10.1029/2025GL118710

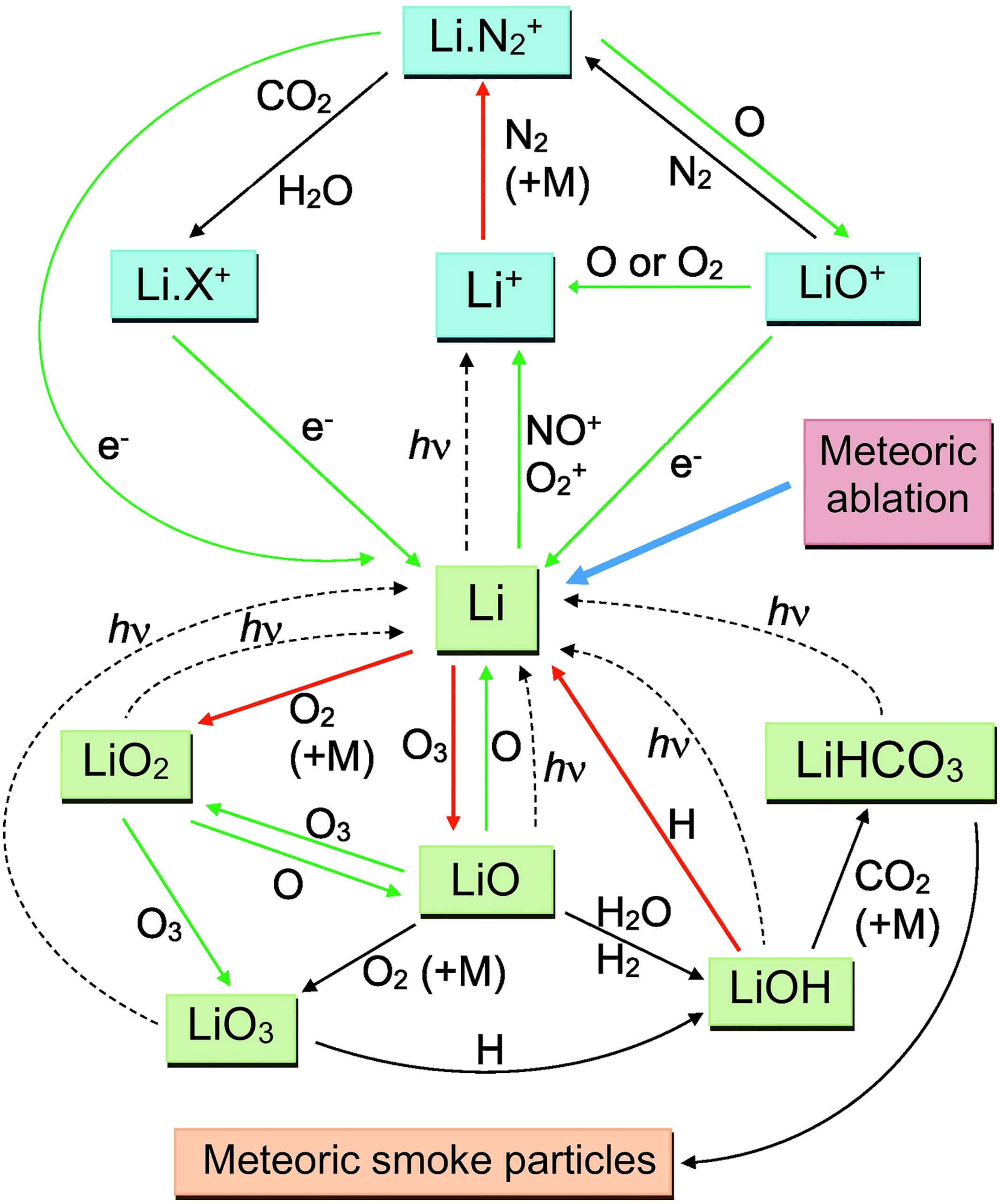

Figure 2. Schematic diagram of the Li chemistry network used in WACCM. The arrows indicate: reactions with measured rate coefficients (red); theoretically calculated rate coefficients (black) and photochemical/photoionization rates (dashed black); rate coefficients set to those of the analogous Na reactions (green); and Li injection rates from meteoric ablation (blue).

(averaged over a solar cycle). The meteoric input function (MIF) of Li, which is the injection rate of Li atoms as a function of height (units: atoms cm^{-3} s^{-1}), is scaled to that of Na by their chondritic ratio (9.77×10^{-4}) (Asplund et al., 2009). The Na meteoric input function was derived by coupling an astronomical model of dust sources in the solar system with the Leeds Chemical Ablation Model (CABMOD) (Carrillo-Sánchez et al., 2020). The resulting injection profiles are illustrated in Figure S6 in Supporting Information S1. As with the other meteoric metals, the Li MIF is reduced in WACCM-Li by a factor of 5 (Plane et al., 2018) to account for the underestimated vertical transport of minor species in the MLT by global models such as WACCM, which do not resolve the short wavelength gravity waves (the horizontal grid scale of the model is ~220 km) that contribute to vertical chemical

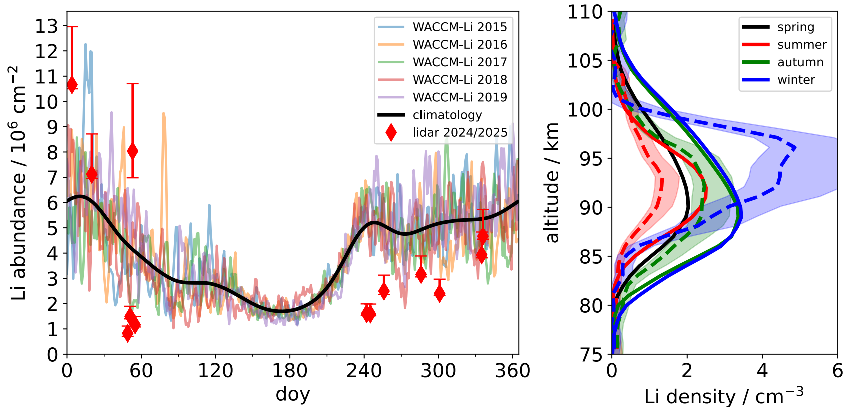

Figure 3. Comparison of lidar observations and WACCM-Li simulations. Left: Variation of Li column abundance throughout the year (diamonds: lidar, August 2024–February 2025). Right: Seasonal mean profiles of Li densities. Dashed: lidar, solid: WACCM-Li. Spring and early summer season are not yet covered by the observations. See text for details.

and dynamical transport of constituents while dissipating (Gardner et al., 2017). Lithium is injected as neutral Li atoms. Although a fraction of these will be converted to Li^+ through impact ionization at hyperthermal speeds, the background ion-molecule chemistry rapidly establishes a steady state between Li and Li^+.

4. Seasonal Variation of Li Abundance in Model and Observations

The Li observations at Kühlungsborn were performed between August 2024 and February 2025. This gives a first impression of the seasonal variation of Li column density that can be compared to WACCM-Li model results. The observed nightly mean Li abundance is shown by the diamonds in Figure 3 (left). Our first soundings in August/September 2024 (day of year, doy, 242/245) revealed a column density of $\sim 1.6 \times 10^6$ cm^{-2}. This value more than doubled during autumn, and by the end of November (doy 335/336), reached $(3.9 - 4.7) \times 10^6$ cm^{-2}. One month later we observed even larger Li column abundance of up to 10.7×10^6 cm^{-2}. But as shown in Figures 1b and 1c, the Li density was highly variable during the night, and the large abundance lasted only for ~2 hr. In February 2025, the Li column density varied by a factor of 10 between 0.8×10^6 cm^{-2} and 8.0×10^6 cm^{-2}, but it should be noted that the large value was observed during the shortest sounding (~1 hr).

WACCM-Li simulates the observed seasonal variation reasonably well. Figure 3 (left) shows the nightly mean values for the individual simulated years. The simulated abundance in summer is about one third of what is calculated in autumn and early winter. The highest values occur at the beginning of the year, where also the short-term variability is largest (up to about a factor of four within a few days). This fits well with the large lidar-observed variability in February 2025. Note that the WACCM-Li simulation covers the years 2015–2019, that is, a detailed agreement with the lidar observations cannot be expected. On the other hand, the described features of the simulated Li abundance are consistent throughout the years. For the climatology, we smoothed all yearly data by a 61-day Hann window and calculated the mean over the five years. By this means we suppressed the large variations in winter in WACCM-Li, which are related to sudden stratospheric warmings (SSW), but do not represent a climatological average. WACCM-Li generally overestimates the observed Li abundance in the second half of the year by about a factor of 1.5–2. Future data will show whether the difference in the timing of the summer-autumn transition between observations and simulations persists.

The lidar observations cover roughly (late) summer, autumn, and winter. Figure 3 (right) shows the respective seasonal averages. In the observations in summer and autumn, the Li density changed strongest below ~90 km, while the peak of the layer stayed at ~92 km. In winter, it rose to 96 km, dominated by the periods of high density shown in Figures 1b and 1c. With WACCM-Li, all data of the different years are averaged with respect to season (spring: March–May, summer: June–August, etc.). Similar to the observations, the FWHM of the layer increases from ~10 km to ~15 km between summer and autumn. The averaged winter profile in WACCM-Li is nearly identical to the autumn profile but averages between lower abundance in December and February and higher abundance in January (cf. Figure 3 left).

5. Discussion and Conclusions

So far, our data set is limited to 13 measurements that lasted between 1 and 7 hr each, with a mean value of 2:40 hr. In the following, we will discuss our observations relative to the soundings at OHP by Jegou et al. (1980, 1985) more than 40 years ago, and to the simulations with WACCM-Li described in Section 4. The Li abundance observed by us between August and December is in satisfactory accord with the data from OHP for the same months ($(1–3) \times 10^6$ cm^{-2}), while on two occasions we detected much higher abundances in January and February (IAP: $>8 \times 10^6$ cm^{-2}, OHP: $<2 \times 10^6$ cm^{-2}). Jegou et al. (1980) suggested a combination of different natural and anthropogenic sources for their Li observations: meteoric ablation, nuclear bomb tests, and Li release experiments. For our soundings, the latter two can be excluded. Therefore, we suggest that the ablation of cosmic dust is the dominating source of the Li layer, at least for the first of our observations. The WACCM-Li results generally confirm this, as they satisfactorily reproduce the observations by considering meteoric ablation only. Additional reasons for Li enhancements are meteor showers, sporadic layers, or the influence of sudden stratospheric warmings (SSW). Single meteoroid ablation plumes usually generate signal peaks of only a few seconds and a few hundred meters (e.g., Höffner et al., 1999) that contribute little to total abundance. Our observation on 3/4 January 2025 coincides with the Quadrantids meteor shower. The cumulative effect during a meteor shower can lead to significant abundance enhancements, but the Li density increased faster and more strongly than observed with other metals during meteor showers (e.g., Gerding et al., 1999).

Sporadic layers may be responsible for the high abundance on 19/20 January 2025, when we also observed a weak sporadic E layer (Es layer) with a nearby (∼120 km distant) ionosonde. On the other hand, there was no signature for Es during the other periods of high Li abundance. The relevance of SSW for the metal abundance has been described by Feng et al. (2017) based on WACCM simulations similar to the methods described here. The short periods with modeled Li column densities of up to 12×10^6 cm^{-2} (cf. Figure 3) are related to post-SSW conditions when the increase in local temperature and changes in circulation lead to an increase of atomic metal concentration (Feng et al., 2017). But under undisturbed winter conditions, the Li column abundance simulated with WACCM-Li remains at about 6×10^6 cm^{-2}. However, the influence of SSW on our observations in January/February 2025 can be ruled out as our co-located RMR temperature soundings do not show a mesospheric cooling related to SSW.

All three potential sources of Li enhancement would have been, in general, also possible at OHP. Nevertheless, the Li abundance in January and February at OHP always remains a factor of 4–5 below our largest values. Therefore, while the low Li abundances observed by lidar in February 2025 are in the range of previous observations and the WACCM-Li simulations, the high values in this period do not appear to be explained by known natural phenomena. It remains speculative whether these events have anthropogenic causes, such as the recently intensified re-entry of Starlink satellites (Space-Track, 2025). Satellites designed for complete demise, like Starlink, are maneuvered in such a way that they experience sufficient drag (SpaceX, 2025) to heat up higher in the atmosphere than satellites making a controlled re-entry above and into the ocean. Future WACCM-Li simulations including the ablation of space debris may be able to explain our observations in early 2025.

In summary, we have successfully conducted Li observations by lidar and developed the first model to examine its natural seasonal variation. More observations are planned to get a better understanding of this still rarely observed metal, especially for a better identification of potential (anthropogenic) trends. Direct observations of metal clouds produced during satellite re-entry in the MLT region, even if rare because of the orbital geometries, will help in understanding the ablation of space debris and assess the future impacts of this new type of atmospheric pollution.

Appendix A: Rate Coefficients

Table A1 lists the rate coefficients for the chemistry network used in WACCM-Li.

Reference to the Notes in the last column of Table A1: 1. Measured (Plane & Helmer, 1994). 2. Set to the rate coefficient for the analogous Na reaction (Plane et al., 2015). 3. Calculated using a Master Equation analysis (for further details, see the SI). 4. Calculated using Transition State Theory (for further details, see the Supporting Information S1). 5. Calculated by detailed balance using the measured rate coefficient for the reverse reaction (Plane & Rajasekhar, 1988a). 6. Measured (Plane & Rajasekhar, 1988b). 7. Reaction is barrierless, so set to a

Table A1
Rate Coefficients for Reactions of Li Species in the Chemistry Network Added to WACCM

No.	Reaction	ΔH_r^o (0 K)[a]	Rate coefficient[b]	Notes
	Neutral reactions			
R1	$Li + O_3 \rightarrow LiO + O_2$	−249.0	$1.1 \times 10^{-9} \exp(-231/T)$	1
R2	$LiO + O \rightarrow Li + O_2$	−141.9	$2.2 \times 10^{-10}(T/200)^{0.5}$	2
R3	$LiO + O_3 \rightarrow LiO_2 + O_2$	−290.0	$1.1 \times 10^{-9} \exp(-570/T)$	2
R4	$LiO + O_2 + M \rightarrow LiO_3$	−119.5	$9.1 \times 10^{-31}(T/200)^{-3.43}$	3
R5a	$LiO + H_2 \rightarrow LiOH + H$	−71.9	$3.9 \times 10^{-11} \exp(-955/T)$	4
R5b	$LiO + H_2 \rightarrow Li + H_2O$	−131.5	$8.6 \times 10^{-12} \exp(-955/T)$	4
R6	$LiO + H_2O \rightarrow LiOH + OH$	−16.3	$1.8 \times 10^{-9}(T/200)^{-0.56}$	3
R7	$LiOH + H \rightarrow Li + H_2O$	−59.6	$6.8 \times 10^{-10} \exp(-716/T)$	5
R8	$LiOH + CO_2 + M \rightarrow LiHCO_3$	−96.1	$1.2 \times 10^{-29}(T/200)^{-3.74}$	3
R9	$Li + O_2 + M \rightarrow LiO_2$	−250.1	$6.3 \times 10^{-30}(T/200)^{-0.93}$	6
R10	$LiO_2 + O \rightarrow LiO + O_2$	−100.8	$5.0 \times 10^{-10} \exp(-940/T)$	2
R11	$LiO_2 + O_3 \rightarrow LiO_3 + O_2$	−118.4	$4.0 \times 10^{-10}(T/200)^{0.5}$	7
R12	$LiO_3 + H \rightarrow LiOH + O_2$	−386.1	$4.0 \times 10^{-10}(T/200)^{0.5}$	7
R13	$LiHCO_3 + LiHCO_3 \rightarrow$ dimer	−191.5	$1.9 \times 10^{-5}(T/200)^{-0.151}$	8
	Ion-molecule reactions			
No.	Reaction	ΔH_r^o (0 K)[a]	Rate coefficient[b]	Notes
R14	$Li + O_2^+ \rightarrow Li^+ + O_2$	−637.9[c]	4.2×10^{-9}	9
R15	$Li + NO^+ \rightarrow Li^+ + NO$	−369.4[d]	1.2×10^{-9}	9
R16	$Li^+ + N_2 + M \rightarrow Li^+ \cdot N_2$	−51.5	$7.6 \times 10^{-30}(T/200)^{-2.17}$[e]	10
R17	$Li^+ + CO_2 + M \rightarrow Li^+ \cdot CO_2$	−81.2	$1.9 \times 10^{-28}(T/200)^{-2.62}$[e]	10
R18	$Li^+ \cdot N_2 + CO_2 \rightarrow LiCO_2^+ + N_2$	−29.7	6.0×10^{-10}	2
R19	$Li^+ \cdot N_2 + O \rightarrow LiO^+ + N_2$	−1.0	4.0×10^{-10}	2
R20	$LiO^+ + N_2 \rightarrow Li^+ \cdot N_2 + O$	+1.0	$4.1 \times 10^{-11}(T/200)^{0.87}$	11
R20	$LiO^+ + O \rightarrow Li^+ + O_2$	−440.2	1.0×10^{-11}	2
R21	$LiO^+ + O_2 \rightarrow Li^+ + O_3$	−49.4	5.0×10^{-12}	2
R22	$Li^+ \cdot X + e^- \rightarrow Li + X$ ($X = N_2, CO_2, O$)	−468.9 (N_2) −439.0 (CO_2) −467.7 (O)	$1.0 \times 10^{-6}(T/200)^{-0.5}$	12
R23	$Li^+ + e^- \rightarrow Li + h\nu$	−520.2	$4.3 \times 10^{-12}(T/200)^{-0.69}$	13
	Photochemical reactions			
No.	Reaction	$\lambda_{threshold}$/nm	Rate coefficient[b]	Notes
J1	$Li + h\nu \rightarrow Li^+ + e^-$	229.9	1.8×10^{-4}	14
J2	$LiO + h\nu \rightarrow Li + O$	340.9	7.8×10^{-3}	15
J3	$LiO_2 + h\nu \rightarrow Li + O_2$	478.3	1.7×10^{-2}	15
J4	$LiO_3 + h\nu \rightarrow LiO + O_2$	1,001	0.13	15
J5	$LiOH + h\nu \rightarrow Li + OH$	278.4	8.5×10^{-4}	15
J6	$LiHCO_3 + h\nu \rightarrow Li + HCO_3$	229.0	3.3×10^{-5}	15

Note. Enthalpy changes and photodissociation thresholds are calculated at the G4 level of theory (Curtiss et al., 2007). [a]kJ mol^{-1}. [b]Units: unimolecular, s^{-1}; bimolecular, cm^3 $molecule^{-1}$ s^{-1}; termolecular, cm^6 $molecule^{-2}$ s^{-1}. [c]Experimental value is −644.4 kJ mol^{-1} (Lide, 2006). [d]Experimental value is −373.7 kJ mol^{-1} (Lide, 2006). [e]Recombination reaction where the rate coefficient measured in He has been multiplied by a factor of 4 to correct for N_2 as third body.

typical collision frequency. 8. The dimerization rate constant is estimated using a Master Equation analysis and then increased by a factor of 1.6×10^4 to allow for polymerization with other metal species (for further details, see the SI). 9. Analogous charge transfer rate coefficient for Na^+ (Plane et al., 2015), scaled by the ratio of the Langevin capture frequencies of Li and Na with NO^+ or O_2^+ (factor = 1.53). 10. Measured (Spears & Ferguson, 1973), and extrapolated to T < 296 K using a Master Equation analysis (for further details, see the SI). 11. Estimate using a Master Equation analysis (for further details, see the SI). 12. Estimate based on review of dissociative electron recombination reactions (Florescu-Mitchell & Mitchell, 2006). 13. Theory calculation (Caves & Dalgarno, 1972). 14. Theory calculation (Verner et al., 1996). 15. Absorption cross section calculated using time-dependent density function theory (TD//B3LYP/6-311+g(2d,p)), convolved with the solar spectral irradiance at λ >180 nm (for further details, see the SI).

Conflict of Interest

The authors declare no conflicts of interest relevant to this study.

Data Availability Statement

The lidar and WACCM-Li data used in the study are available at Gerding et al. (2025).

Acknowledgments
Ionosonde data was kindly provided by our colleague Jens Mielich. We thank our colleagues Torsten Köpnick and Reik Ostermann for their help with the lidar electronics, Josef Höffner for provision of the data acquisition software, and Michael Priester for his help for maintaining the laser. J.M.C.P. and W.F. were supported by the European Space Agency and UK Space Agency (EISI agreement 4000146844). Open Access funding enabled and organized by Projekt DEAL.

References

Asplund, M., Grevesse, N., Sauval, A. J., & Scott, P. (2009). The chemical composition of the Sun. *Annual Review of Astronomy and Astrophysics*, *47*(1), 481–522. https://doi.org/10.1146/annurev.astro.46.060407.145222

Barker, C. R., Marais, E. A., & McDowell, J. C. (2024). Global 3D rocket launch and re-entry air pollutant and CO_2 emissions at the onset of the megaconstellation era. *Scientific Data*, *11*(1), 1079. https://doi.org/10.1038/s41597-024-03910-z

Boley, A. C., & Byers, M. (2021). Satellite mega-constellations create risks in Low Earth Orbit, the atmosphere and on Earth. *Scientific Reports*, *11*(1), 10642. https://doi.org/10.1038/s41598-021-89909-7

Carrillo-Sánchez, J. D., Gómez-Martín, J. C., Bones, D. L., Nesvorný, D., Pokorný, P., Benna, M., et al. (2020). Cosmic dust fluxes in the atmospheres of Earth, Mars, and Venus. *Icarus*, *335*, 113395. https://doi.org/10.1016/j.icarus.2019.113395

Caves, T., & Dalgarno, A. (1972). Model potential calculations of lithium transitions. *Journal of Quantitative Spectroscopy and Radiative Transfer*, *12*(11), 1539–1552. https://doi.org/10.1016/0022-4073(72)90129-X

Chen, Y., & Chu, X. (2023). Lidar observations of predawn thermosphere-ionosphere Na (TINa) layers over boulder (40.13°N, 105.24°W): Annual phase variations and correlation with sunrise and tidal winds. *Geophysical Research Letters*, *50*(18), e2023GL105626. https://doi.org/10.1029/2023gl105626

Chu, X., Huang, W., Fong, W., Yu, Z., Wang, Z., Smith, J. A., & Gardner, C. S. (2011). First lidar observations of polar mesospheric clouds and Fe temperatures at McMurdo (77.8°S, 166.7°E), Antarctica. *Geophysical Research Letters*, *38*(16). https://doi.org/10.1029/2011GL048373

Chu, X., & Papen, G. (2005). Resonance fluorescence lidar for measurements of the middle and upper atmosphere. In T. Fujii & T. Fukuchi (Eds.), *Laser remote sensing* (pp. 179–468). Taylor & Francis.

Curtiss, L. A., Redfern, P. C., & Raghavachari, K. (2007). Gaussian-4 theory. *Journal of Chemical Physics*, *126*(8), 084108. https://doi.org/10.1063/1.2436888

Danabasoglu, G., Lamarque, J.-F., Bacmeister, J., Bailey, D. A., DuVivier, A. K., Edwards, J., et al. (2020). The Community Earth System Model Version 2 (CESM2). *Journal of Advances in Modeling Earth Systems*, *12*(2), e2019MS001916. https://doi.org/10.1029/2019MS001916

Feng, W., Kaifler, B., Marsh, D. R., Höffner, J., Hoppe, U.-P., Williams, B. P., & Plane, J. M. (2017). Impacts of a sudden stratospheric warming on the mesospheric metal layers. *Journal of Atmospheric and Solar-Terrestrial Physics*, *162*, 162–171. https://doi.org/10.1016/j.jastp.2017.02.004

Feng, W., Marsh, D. R., Chipperfield, M. P., Janches, D., Höffner, J., Yi, F., & Plane, J. M. C. (2013). A global atmospheric model of meteoric iron. *Journal of Geophysical Research*, *118*(16), 9456–9474. https://doi.org/10.1002/jgrd.50708

Ferreira, J. P., Huang, Z., Nomura, K.-I., & Wang, J. (2024). Potential ozone depletion from satellite demise during atmospheric reentry in the era of mega-constellations. *Geophysical Research Letters*, *51*(11), e2024GL109280. https://doi.org/10.1029/2024GL109280

Florescu-Mitchell, A., & Mitchell, J. (2006). Dissociative recombination. *Physics Reports*, *430*(5–6), 277–374. https://doi.org/10.1016/j.physrep.2006.04.002

Fricke, K., & von Zahn, U. (1985). Mesopause temperatures derived from probing the hyperfine structure of the D_2 resonance line of sodium by lidar. *Journal of Atmospheric and Terrestrial Physics*, *47*(5), 499–512. https://doi.org/10.1016/0021-9169(85)90116-3

Frisch, M. J., Trucks, G. W., Schlegel, H. B., Scuseria, G. E., Robb, M. A., Cheeseman, J. R., et al. (2016). *Gaussian 16*. Gaussian, Inc. Wallingfort.

Gadsden, M., & Salmon, K. (1958). Presence of 6707 A. Radiation in the twilight sky. *Nature*, *182*(4649), 1598–1599. https://doi.org/10.1038/1821598a0

Gardner, C. S., Liu, A. Z., & Guo, Y. (2017). Vertical and horizontal transport of mesospheric Na: Implications for the mass influx of cosmic dust. *Journal of Atmospheric and Solar-Terrestrial Physics*, *162*, 192–202. https://doi.org/10.1016/j.jastp.2016.07.013

Georgievskii, Y., & Klippenstein, S. J. (2005). Long-range transition state theory. *Journal of Chemical Physics*, *122*(19), 194103. https://doi.org/10.1063/1.1899603

Gerding, M., Alpers, M., Höffner, J., & Von Zahn, U. (1999). Simultaneous K and Ca lidar observations during a meteor shower on March 6–7, 1997, at Kühlungsborn, Germany. *Journal of Geophysical Research*, *104*(A11), 24689–24698. https://doi.org/10.1029/1999JA900338

Gerding, M., Daly, S., & Plane, J. M. C. (2019). Lidar soundings of the mesospheric nickel layer using $Ni(^3F)$ and $Ni(^3D)$ transitions. *Geophysical Research Letters*, *46*(1), 408–415. https://doi.org/10.1029/2018GL080701

Gerding, M., Kopp, M., Höffner, J., Baumgarten, K., & Lübken, F.-J. (2016). Mesospheric temperature soundings with the new, daylight-capable IAP RMR lidar. *Atmospheric Measurement Techniques*, *9*(8), 3707–3715. https://doi.org/10.5194/amt-9-3707-2016

Gerding, M., Wing, R., Feng, W., Plane, J. M. C., & Baumgarten, G. (2025). New lithium lidar observations and model simulations: A window to anthropogenic signatures [Dataset]. https://doi.org/10.22000/phkjdccwkwjazpnm

Gerding, M., Wing, R., Franco-Diaz, E., Baumgarten, G., Fiedler, J., Köpnick, T., & Ostermann, R. (2024). The Doppler wind, temperature, and aerosol RMR lidar system at Kühlungsborn, Germany – Part 1: Technical specifications and capabilities. *Atmospheric Measurement Techniques*, *17*(9), 2789–2809. https://doi.org/10.5194/amt-17-2789-2024

Gettelman, A., Mills, M. J., Kinnison, D. E., Garcia, R. R., Smith, A. K., Marsh, D. R., et al. (2019). The whole atmosphere community climate model version 6 (WACCM6). *Journal of Geophysical Research*, *124*(23), 12380–12403. https://doi.org/10.1029/2019JD030943

Glowacki, D. R., Liang, C.-H., Morley, C., Pilling, M. J., & Robertson, S. H. (2012). MESMER: An open-source master equation solver for multi-energy well reactions. *Journal of Physical Chemistry A*, *116*(38), 9545–9560. https://doi.org/10.1021/jp3051033

Guo, Y., Liu, A. Z., & Gardner, C. S. (2017). First Na lidar measurements of turbulence heat flux, thermal diffusivity, and energy dissipation rate in the mesopause region. *Geophysical Research Letters*, *44*(11), 5782–5790. https://doi.org/10.1002/2017gl073807

Höffner, J., & Lautenbach, J. (2009). Daylight measurements of mesopause temperature and vertical wind with the mobile scanning iron lidar. *Optics Letters*, *34*(9), 1351. https://doi.org/10.1364/OL.34.001351

Höffner, J., Von Zahn, U., McNeil, W. J., & Murad, E. (1999). The 1996 Leonid shower as studied with a potassium lidar: Observations and inferred meteoroid sizes. *Journal of Geophysical Research*, *104*(A2), 2633–2643. https://doi.org/10.1029/1998JA900063

Huang, W., Chu, X., Gardner, C. S., Carrillo-Sánchez, J. D., Feng, W., Plane, J. M. C., & Nesvorný, D. (2015). Measurements of the vertical fluxes of atomic Fe and Na at the mesopause: Implications for the velocity of cosmic dust entering the atmosphere. *Geophysical Research Letters*, *42*(1), 169–175. https://doi.org/10.1002/2014GL062390

Jegou, J.-P., Chanin, M.-L., Mégie, G., & Blamont, J. E. (1980). Lidar measurements of atmospheric lithium. *Geophysical Research Letters*, *7*(11), 995–998. https://doi.org/10.1029/GL007i011p00995

Jegou, J. P., Granier, C., Chanin, M. L., & Megie, G. (1985). General theory of the alkali metals present in the earth's upper atmosphere. I - Flux model: Chemical and dynamical processes. *Annals of Geophysics*, *3*, 163–175.

Lautenbach, J., Höffner, J., Lübken, F.-J., Kopp, M., & Gerding, M. (2017). Ten-year climatology of potassium number density at 54°N, 12°E. *Journal of Atmospheric and Solar-Terrestrial Physics*, *162*, 172–177. https://doi.org/10.1016/j.jastp.2017.06.010

Lide, D. R. (2006). *CRC handbook of chemistry and physics: A ready-reference book of chemical and physical data* (87th ed.). CRC Press. https://doi.org/10.1021/ja069813z

Matthes, K., Funke, B., Andersson, M. E., Barnard, L., Beer, J., Charbonneau, P., et al. (2017). Solar forcing for CMIP6 (v3.2). *Geoscientific Model Development*, *10*(6), 2247–2302. https://doi.org/10.5194/gmd-10-2247-2017

Molod, A., Takacs, L., Suarez, M., & Bacmeister, J. (2015). Development of the GEOS-5 atmospheric general circulation model: Evolution from MERRA to MERRA2. *Geoscientific Model Development*, *8*(5), 1339–1356. https://doi.org/10.5194/gmd-8-1339-2015

Murphy, D. M., Abou-Ghanem, M., Cziczo, D. J., Froyd, K. D., Jacquot, J., Lawler, M. J., et al. (2023). Metals from spacecraft reentry in stratospheric aerosol particles. *Proceedings of the National Academy of Sciences of the United States of America*, *120*(43), e2313374120. https://doi.org/10.1073/pnas.2313374120

NIST. (2025). Persistent lines of neutral lithium (Li I). (last access 2025-07-21) Retrieved from https://physics.nist.gov/PhysRefData/Handbook/Tables/lithiumtable3.htm

Phillips, M. C., Kautz, E. J., & Harilal, S. S. (2025). Detection limits for laser absorption spectroscopy of Li in laser ablation plumes. *Optics Letters*, *50*(10), 3349. https://doi.org/10.1364/OL.564323

Picone, J. M., Hedin, A. E., Drob, D. P., & Aikin, A. C. (2002). NRLMSISE-00 empirical model of the atmosphere: Statistical comparisons and scientific issues. *Journal of Geophysical Research*, *107*(A12). https://doi.org/10.1029/2002JA009430

Plane, J. M. C., & Helmer, M. (1994). Laboratory studies of the chemistry of meteoric metals. In G. Hancock & R. G. Compton (Eds.), *Research in chemical kinetics* (pp. 313–367). Elsevier.

Plane, J. M. C., Feng, W., & Dawkins, E. C. M. (2015). The mesosphere and metals: Chemistry and changes. *Chemical Reviews*, *115*(10), 4497–4541. https://doi.org/10.1021/cr500501m

Plane, J. M. C., Feng, W., Gómez Martín, J. C., Gerding, M., & Raizada, S. (2018). A new model of meteoric calcium in the mesosphere and lower thermosphere. *Atmospheric Chemistry and Physics*, *18*(20), 14799–14811. https://doi.org/10.5194/acp-18-14799-2018

Plane, J. M. C., & Rajasekhar, B. (1988a). Study of the reaction Li + H_2 O over the temperature range 850–1000 K by time-resolved laser-induced fluorescence of Li(2^2 P_J -2^2 $S_{1/2}$). *Journal of the Chemical Society, Faraday Transactions 2*, *84*(3), 273–285. https://doi.org/10.1039/F29888400273

Plane, J. M. C., & Rajasekhar, B. (1988b). A study of the reaction Li + O_2 + M (M = N_2, He) over the temperature range 267-1100 K by time-resolved laser-induced fluorescence of Li(22PJ-22S1/2). *Journal of Physical Chemistry*, *92*(13), 3884–3890. https://doi.org/10.1021/j100324a041

Schulz, L., & Glassmeier, K.-H. (2021). On the anthropogenic and natural injection of matter into Earth's atmosphere. *Advances in Space Research*, *67*(3), 1002–1025. https://doi.org/10.1016/j.asr.2020.10.036

Space-Track. (2025). Space-track. Retrieved from https://www.space-track.org/#decay

SpaceX. (2025). Starlink satellite demisability. (last access 2025-03-24) Retrieved from https://www.starlink.com/public-files/Starlink_Approach_to_Satellite_Demisability.pdf

Spears, K. G., & Ferguson, E. E. (1973). Termolecular and saturated termolecular kinetics for Li^+ and F^-. *Journal of Chemical Physics*, *59*(8), 4174–4183. https://doi.org/10.1063/1.1680610

Sullivan, H. M., & Hunten, D. M. (1962). Lithium twilight at Saskatoon, 1960–61. *Nature*, *193*(4820), 1064–1065. https://doi.org/10.1038/1931064a0

Tobiska, W., Woods, T., Eparvier, F., Viereck, R., Floyd, L., Bouwer, D., et al. (2000). The SOLAR2000 empirical solar irradiance model and forecast tool. *Journal of Atmospheric and Solar-Terrestrial Physics*, *62*(14), 1233–1250. https://doi.org/10.1016/S1364-6826(00)00070-5

Verner, D. A., Ferland, G. J., Korista, K. T., & Yakovlev, D. G. (1996). Atomic data for astrophysics. II. New analytic FITS for photoionization cross sections of atoms and ions. *The Astrophysical Journal*, *465*, 487. https://doi.org/10.1086/177435

Wiese, W. L., & Fuhr, J. R. (2009). Accurate atomic transition probabilities for hydrogen, helium, and lithium. *Journal of Physical and Chemical Reference Data*, *38*(3), 565–720. https://doi.org/10.1063/1.3077727

Wu, F., Zheng, H., Yang, Y., Cheng, X., Li, F., Du, L., et al. (2021). Lidar observations of the upper atmospheric nickel layer at Beijing (40°N,116°E). *Journal of Quantitative Spectroscopy and Radiative Transfer*, *260*, 107468. https://doi.org/10.1016/j.jqsrt.2020.107468

Zander, F., & Löhle, S. (2025). A review of airborne observations for space debris re-entry break-up and dispersion measurements. *CEAS Space J*, *17*(6), 1019–1030. https://doi.org/10.1007/s12567-025-00608-9